Nitrogenase Catalytic Cofactor Indicates That the CFe_6 Core Is a Stabilizing "Heart of Steel"

Dmitriy A. Lukoyanov, Zhi-Yong Yang, Ana Pérez-González, Simone Raugei,* Dennis R. Dean,* Lance C. Seefeldt,* and Brian M. Hoffman*

ABSTRACT: Substrates and inhibitors of Mo-dependent nitrogenase bind and react at Fe ions of the active-site FeMo-cofactor [7Fe−9S−C−Mo−homocitrate] contained within the MoFe protein α-subunit. The cofactor contains a CFe_6 core, a carbon centered within a trigonal prism of six Fe, whose role in catalysis is unknown. Targeted ^{13}C labeling of the carbon enables electron-nuclear double resonance (ENDOR) spectroscopy to sensitively monitor the electronic properties of the Fe−C bonds and the spin-coupling scheme adopted by the FeMo-cofactor metal ions. This report compares $^{13}CFe_6$ ENDOR measurements for (i) the wild-type protein resting state (E_0; α-Val^{70}) to those of (ii) α-Ile^{70}, (iii) α-Ala^{70}-substituted proteins; (iv) crystallographically characterized CO-inhibited "hi-CO" state; (v) $E_4(4H)$ Janus intermediate, activated for N_2 binding/reduction by accumulation of 4[e^-/H^+]; (vi) $E_4(2H)^*$ state containing a doubly reduced FeMo-cofactor without Fe-bound substrates; and (vii) propargyl alcohol reduction intermediate having allyl alcohol bound as a ferracycle to FeMo-cofactor Fe6. All states examined, both $S = 1/2$ and $3/2$ exhibited near-zero ^{13}C isotropic hyperfine coupling constants, ${}^{C}a = [-1.3 \leftrightarrow +2.7]$ MHz. Density functional theory computations and natural bond orbital analysis of the Fe−C bonds show that this occurs because a (3 spin-up/3 spin-down) spin-exchange configuration of CFe_6 Fe-ion spins produces cancellation of large spin-transfers to carbon in each Fe−C bond. Previous X-ray diffraction and DFT both indicate that trigonal-prismatic geometry around carbon is maintained with high precision in all these states. The persistent structure and Fe−C bonding of the CFe_6 core indicate that it does not provide a functionally dynamic (hemilabile) "beating heart"—instead it acts as "a heart of steel", stabilizing the structure of the FeMo-cofactor-active site during nitrogenase catalysis.

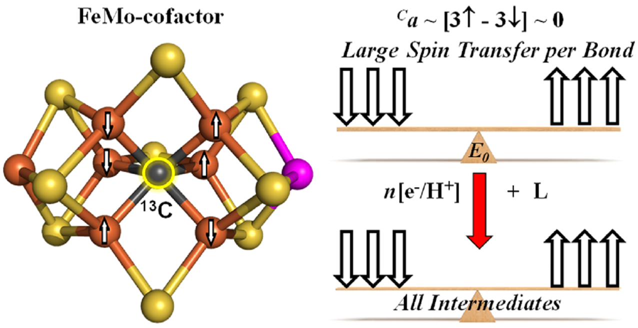

INTRODUCTION

All known diazotrophic organisms produce a Mo-dependent nitrogenase that catalyzes the ATP-dependent reduction of N_2, yielding two NH_3.[1] Substrate activation and reduction occur on a Fe_7MoS_9C−homocitrate metallocluster, designated FeMo-cofactor (Figure 1), contained within the α-subunit of the MoFe protein component of nitrogenase. Activation of FeMo-cofactor for substrate binding and reduction involves the sequential accumulation of electrons and protons. The progressive steps are denoted E_n, $n = 0$−8 for the number of e^-/H^+ additions to the E_0 resting state, with proton or substrate moieties when known, indicated in parentheses.[2,3] For example, $E_2(2H)$ indicates a species that has accumulated two electrons and two protons relative to the E_0 state.[4,5] Other than the physiological substrate N_2, there are a variety of other substrates (i.e., alkynes) and inhibitors (i.e., CO) that bind to the FeMo-cofactor, and these have long been used to explore the catalytic mechanism.[6]

Substrate and inhibitor binding to the FeMo-cofactor occurs at Fe ions of the FeMo-cofactor (Figure 1A,B) that form a trigonal prismatic CFe_6 core having a central carbon (Figure 1C).[7] This core resembles the structural motif of cementite, the constituent of steels that gives them toughness.[8−10] Such a carbon-containing core is unprecedented in biological cofactors, and its function during nitrogenase catalysis remains unknown. At one extreme, the Fe−C bonds could provide a functionally dynamic (hemilabile) "beating heart", weakening or breaking to allow substrate or inhibitor binding to the associated Fe atom (Figure 1D) (e.g., ref 11). Such behavior might underlie our observations that all intermediates trapped to date beyond the $E_2(2H)$ state of the catalytic cycle have been converted from the $S = 3/2$ spin state of E_0 to $S = 1/2$

Received: June 10, 2022

https://doi.org/10.1021/jacs.2c06149

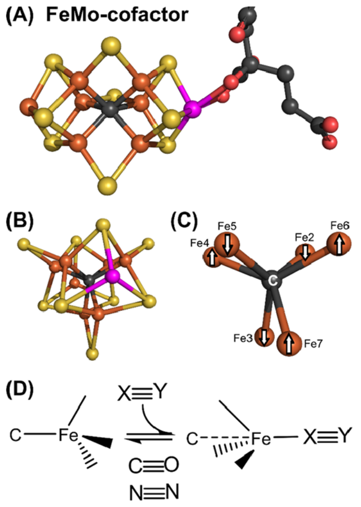

Figure 1. FeMo-cofactor; Fe (orange), Mo (purple), S (yellow), C (gray), O (red). (A) Full view. (B) End-on view of the $[Fe_7MoS_9C]$ cluster. (C) End-on view of the CFe_6 core with (3↑/3↓) BS7 spin projections. (D) Cartoon of the hemilabile Fe−C bond.

spin states, with differing g-values[6,12] and FeMo-cofactor ^{57}Fe hyperfine couplings.[13,14] At the other extreme, the CFe_6 core could be acting as a "heart of steel" that retains its structure and stabilizes the FeMo-cofactor as the enzyme progresses along the substrate binding and reduction pathway. To explore the function of the carbon-containing CFe_6 core in catalysis and to distinguish between the alternative possibilities for its role, a procedure for targeted labeling of the carbon with ^{13}C was developed to enable electron nuclear double resonance (ENDOR) spectroscopy to sensitively and precisely monitor the electronic properties of the Fe−C bonding, and through this, the spin-coupling scheme is adopted by the FeMo-cofactor metal ions.[15]

Using this approach, we previously observed that in the $S = 3/2$ E_0 resting state, despite direct bonding between the FeMo-cofactor carbon and its six surrounding high-spin Fe ions, the $^{13}CFe_6$ core surprisingly exhibits a near-zero net ^{13}C isotropic coupling constant, $^{C}a = +0.86$ MHz; to put this value in perspective, the textbook value for the isotropic coupling associated with one electron in a carbon 2s orbital is $a_{2S} \approx 3800$ MHz.[16,17] This unexpected observation was explained through the recognition that the FeMo-cofactor metal-ion spins exhibit an exchange-coupling scheme with three of the six "belt" Fe ions of the CFe_6 FeMo-cofactor core bonded to the carbon being "spin-up (↑)" and three "spin-down (↓)", schematically denoted (3↑/3↓), an arrangement previously designated as BS7 by Noodleman and Case.[18] In this configuration, the sum of the positive contributions to the ^{13}C spin density from the three belt "spin-up Fe" ions is cancelled by the sum of negative contributions from the three belt "spin-down Fe" ions (Figure 1C), resulting in the observed near-zero value for the ^{13}C isotropic hyperfine coupling constant, ^{C}a. Perhaps more surprisingly, the magnitude of the isotropic coupling changes little when nitrogenase is trapped in a CO-bound, $S = 1/2$ state denoted hi-CO during turnover under high pressure of the inhibitor CO.[19] It has been crystallographically established that the FeMo-cofactor in the hi-CO state has two bound CO molecules.[20] As indicated in Scheme 1B, one CO binds to Fe6 and the other is bridged between Fe2 and Fe6, replacing the sulfide (S2B) that bridges these Fe ions in E_0 (Scheme 1A). This invariance of ^{C}a upon conversion to hi-CO was interpreted to indicate that this state also exhibits a BS7-type (3↑/3↓) configuration of electron spins on the six Fe-ions of the CFe_6 trigonal-prism analogous to that of E_0, even though the FeMo-cofactor has bound two CO molecules to Fe atoms of the core, has lost the sulfide S2B that bridges Fe2/Fe6, and has undergone a change in the spin state ($S = 3/2 \rightarrow 1/2$). This result established that the ^{13}C ENDOR measurement of ^{C}a for the ^{13}C-labeled FeMo-cofactor could indeed serve as a basis for evaluating spin-exchange models and Fe−C bonding in freeze-trapped enzymatic intermediates.

Scheme 1. Cartoon of the Fe2367 FeMo-Cofactor Face for Relevant States

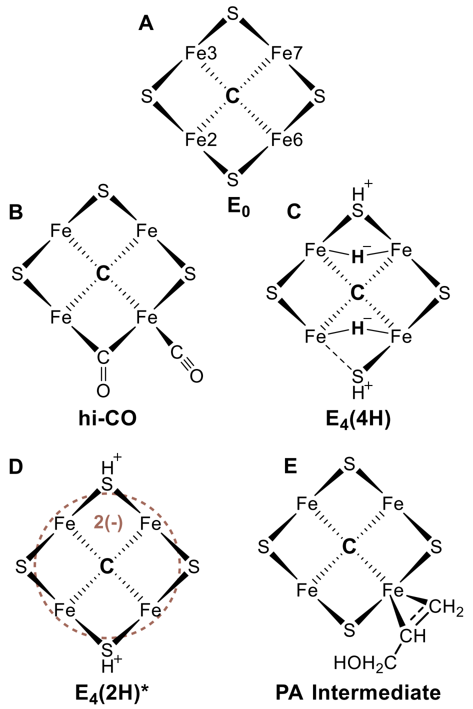

The present work compares ENDOR measurements of the ^{13}C carbon hyperfine coupling in multiple resting and freeze-trapped, turnover states, Scheme 1. The ability to examine the CFe_6 core of the FeMo-cofactor in a wide variety of different states is introduced by targeted ^{13}C labeling of wild-type and variant forms of the MoFe protein having an amino acid substitution within the first shell of a non-covalent interaction with the FeMo-cofactor. The variant MoFe proteins used here have either the α-Val^{70} residue substituted by α-Ala^{70} or by α-Ile^{70}.[21] Hereafter, the MoFe protein having no amino acid substitutions is designated as a wild-type (WT) protein and the MoFe protein having the α-Val^{70} residue substituted by either Ile or Ala is, respectively, designated as either the α-Ile^{70} protein or the α-Ala^{70} protein. As indicated below, the ^{13}C-labeled α-Ile^{70} protein has been used to trap the labeled E_4(4H) state under conditions of proton reduction[22−24] and a state denoted E_4(2H)* containing a doubly reduced FeMo-cofactor without Fe-bound substrates.[14,25] The ^{13}C-labeled α-Ala^{70} protein has been used to capture a reduction intermediate of the large alkyne substrate propargyl alcohol (PA).[26−28]

The principal experimental outcomes of this study are to determine the exchange-coupling scheme exhibited by the

FeMo-cofactor in trapped intermediates, in particular, determining whether this changes from the ($3\uparrow/3\downarrow$) scheme of E_0, and likewise to test for loss of Fe−C bonding within and geometry of the CFe_6 core of the intermediates. The components of this study are as follows. (i) Comparison among E_0 states of variant MoFe proteins. (ii) Further comparison of WT E_0 to the crystallographically characterized WT hi-CO state (Scheme 1A,B). (iii) Characterization of the E_4(4H) state of the FeMo-cofactor produced by the α-Ile[70] protein (Scheme 1C). (iv) Analysis of a species produced by photochemical reductive elimination of H_2 from E_4(4H) without the associated binding of N_2. This state of the FeMo-cofactor is designated E_4(2H)* (Scheme 1D). (v) Characterization of a species produced by the α-Ala[70] protein that contains a PA reduction intermediate (Scheme 1E). (vi) Examination of the states studied through density functional theory (DFT) computations and natural bond orbital (NBO) analysis[29] of the Fe−C bonds in their CFe_6 cores.

Several of these states are of particularly high mechanistic significance. E_4(4H) is the key activated state required to achieve perhaps the most challenging transformation in biology: cleavage of the N≡N triple bond. Binding of N_2 must be preceded by the accumulation of four electrons and protons by the FeMo-cofactor to form E_4(4H). In this state, the four electrons are associated with two hydrides that bridge irons of the FeMo-cofactor and two protons likely residing on bridging sulfurs,[24] resulting in a formal charge on the metal-ion core equal to that of the E_0 state. We note that details of the structure of the FeMo-cofactor of E_4(4H), with its two bridging hydrides as shown in Scheme 1C, are the subject of the current discussion (e.g., refs 30 and 31). N_2 binding/reduction at the iron core of the FeMo-cofactor is mechanistically coupled to, and thermodynamically driven by, the reductive elimination of two hydrides, the result being the formation of the first intermediate of N_2 reduction, E_4(2N2H), which contains N_2 at the redox level of diazene.[12,32] E_4(2H)* (Scheme 1D) represents the "chemically simplest" intermediate in which the Fe framework is doubly reduced and two sulfides are protonated.[14,25] The PA intermediate represents an organometallic analogue to the diazene-level E_4(2N2H) state in which the alkene reduction product forms a ferracycle with Fe6 (Scheme 1E).[26] The experimental results are illuminated by DFT analysis of the cofactor electronic and geometric structure in the E_0 resting state, the hi-CO, E_4(4H), E_4(2H)*, and PA intermediates, and, beyond that, of an inferred H_2-bound transient intermediate in the conversion of E_4(4H) to E_4(2H)* + H_2.[33]

The combination of experiment and quantum computation on this diverse set of nitrogenase states leads to an answer for the fundamental question: does the CFe_6 FeMo-cofactor core provide a functionally dynamic (hemilabile) "beating heart" that facilitates substrate binding/reduction through weakening Fe−C bond(s) (Figure 1D), or is it a structurally persistent "heart of steel", stabilizing the FeMo-cofactor during nitrogenase catalysis, as formulated by Prof. Oliver Einsle.[34]

INTRODUCTION

Targeted Labeling of the FeMo-Cofactor. *A. vinelandii* strains DJ2396 (WT), DJ2399 (MoFe α-Ile[70]), and DJ2435 (MoFe α-Ala[70]) were used for ^{13}C-labeling experiments. These strains contain a Strep-tag-encoding sequence placed at the N-terminus of the MoFe protein α-subunit for affinity purification purposes and a streptomycin resistance-encoding gene cartridge disrupting the *metZ* gene.[15] For large-scale cultures, cells were grown in a 150 L custom-built fermenter (W.B. Moore, Inc., Easton, PA) at 30 °C in a modified Burk medium supplemented with 5.7 mM ammonium acetate as a fixed nitrogen source. Once the fixed nitrogen source was exhausted, cells were cultured for an additional 4 h and harvested. The culture medium was supplemented with 50 μg/mL L-methionine-(methyl-^{13}C) for obtaining ^{13}C-labeling MoFe protein samples (Sigma-Aldrich) and 50 μg/mL L-methionine (Sigma-Aldrich). Affinity-tagged MoFe proteins were purified as previously described.[35,36] Similarly, resting-state and turnover samples were prepared as described previously.[14,15,22,26,33]

ENDOR. *Q*-Band 2 K ENDOR spectra were collected as discussed previously.[15] The ^{13}C ENDOR response for a single orientation of the magnetic field relative to the FeMo-cofactor is a doublet centered at the Larmor frequency and split by the orientation-dependent hyperfine coupling. ^{13}C carbon hyperfine tensors for a given state are determined by analysis of two-dimensional (2D) field-frequency plots of ENDOR spectra collected across the electron paramagnetic resonance (EPR) envelope of that state.[37,38] The choice of continuous wave (CW) versus pulsed ENDOR technique is made on considerations of both signal/noise, with CW invariably being more sensitive, and signal shape. Pulsed spectra are frequently better-resolved but are subject to well-understood response functions that must be incorporated.[39] In particular, the intensity of a Mims ENDOR spectrum is modulated by the response function, $I(A) \sim [1 - \cos(2\pi A\tau)]$, where A is a hyperfine coupling and τ is the pulse interval in the Mims ENDOR electron spin-echo sequence.[40] CW spectra commonly are subject to relaxation distortions understood since Feher's invention of ENDOR, and this is the case here. In a frequency-swept ENDOR spectrum that exhibits these effects, the "leading edge" of a peak, the edge first encountered by the RF sweep, is well-defined, but the response persists and "tails off" after the frequency has moved past the peak, so that the trailing edge is not well-defined. Thus, the shape of the same "peak" can be quite different for a frequency-swept CW ENDOR spectrum swept from a low−high frequency from that swept high−low, with both different from the peak in a pulsed ENDOR measurement.

DFT Calculations. DFT calculations were performed on the models of the FeMo-cofactor environment described previously[41] using the same geometry constraints described there. These models fully consider the network of interactions (e.g., hydrogen-bonding, electrostatic, van der Waals) at the active site as inferred from molecular dynamic simulations[42] initiated from the crystal structure of the E_0 state (Protein Data Bank entry 3U7Q).[7] We considered the E_0 (S = 3/2) resting state, the hi-CO (S = 1/2) species, and the E_4(4H), E_4(H_2,2H), and E_4(2H)* (all S = 1/2) intermediates. All calculations were performed starting from E_0 in the oxidation state [$Mo^{3+}3Fe^{2+}4Fe^{3+}$] with all metal centers in a high-spin configuration. All calculations presented in this work were performed on E_0 in this oxidation state. If we do not distinguish the specific location of Fe^{2+} and Fe^{3+} centers, we have a total of 7!/(4!·3!) = 35 possible spin-up and spin-down combinations for both S = 1/2 and 3/2 total spin states. All 35 spin coupling patterns were investigated using both the BP86[43−45] and B3LYP[46−48] exchange and correlation functionals. The two functionals provide a similar overall picture and, in the text, only BP86 results are discussed. The def2-TZVP basis set[49] was adopted for all atoms with the addition of an effective core potential for Mo.[50] As discussed elsewhere,[30,41,51−53] the lowest-energy solutions maximize the antiferromagnetic coupling, resulting in a ($3\uparrow/3\downarrow$) coupling scheme. Results are explicitly discussed for the lowest-energy states. Similar results are obtained for the other low-lying solutions. All calculations were performed with the program ORCA5.0.[54,55] The coordinates of all models are given in the Supporting Information.

Distortions of the CFe_6 core geometry $\mathbf{r}$ from the ideal prismatic (D_{3h}) symmetry were quantified by the order parameter

$$O(D_{3h}) = \frac{1}{N}\sum_{R} \|R(\mathbf{r}) - \mathbf{r}\|$$

Table 1. g-Values and ^{13}C Hyperfine Parameters for the Nitrogenase Resting and Intermediate States

		E_0(WT)[a]	hi-CO	E_4(2H)*	E_4(4H)	PA
g	**g_1**	4.30	**2.17**	**2.098**	**2.15**	**2.127**
	g_2	3.67	2.06	2.00	2.007	2.004
	g_3	**2.01**		1.956	1.965	1.991
	$^{C}\boldsymbol{a}$	**+0.86**	**−1.30**	**|0.9|**[c]	**+2.7**	**|2.3|**[c]
$^{C}\boldsymbol{A}$[b]	A_1	+3.10	+3.2	3.6	+6.3	5.5
	A_2	+0.43	−3.4	0.8	0	1.3
	A_3	−0.95	−3.7	−1.6	+1.9	0
$^{C}\boldsymbol{T}$[b]	T_1	+2.24	+4.5	+2.7	+3.6	+3.2
	T_2	−0.43	−2.1	−0.1	−2.7	−1.0
	T_3	−1.81	−2.4	−2.5	−0.8	−2.3
	$^{C}\boldsymbol{T}$ symmetry	***Rhombic***	***Dipolar***	***Rhombic***	***Rhombic***	***Rhombic***

[a] $S = 3/2$; effective-spin 1/2 g'-values tabulated. All other states, $S = 1/2$. Bold, $g_{\parallel}$. [b] All hyperfine parameters in MHz. [c] Only relative signs of the ^{13}C carbon $^{C}\boldsymbol{A}$ and $^{C}\boldsymbol{T}$ hyperfine tensors, and thus $|^{C}a|$, are known.

where the summation runs over all the N symmetry operations R of the D_{3h} space group ($2C_3$, $3C_2$, σ_h, $2S_3$; see Scheme S2). The symmetry axes C_3 and S_3 are defined as the line passing through the geometric center of the trigonal bases, the three C_2 axes as the lines perpendicular to each of the three rectangular sides and passing through the geometric center, and the σ_h plane as the plane perpendicular to C_3 bisecting the prism. For a perfectly prismatic structure, $O(D_{3h}) = 0$.

The bonding properties of the CFe_6 FeMo-cofactor core were investigated within the NBO framework.[29] This framework allows the degrees of covalency of a chemical bond to be quantified in terms of concepts similar to Lewis chemical structures. In the NBO formulation, the covalent bond, ϕ, between two atoms A and B, is formed by a linear combination of two natural hybrid orbitals, h_A and h_B, defined in terms of effective valence-shell (natural) atomic orbitals centered on A and B, optimized for maximum occupancy

$$\phi = c_A h_A + c_B h_B$$

where $|c_A|^2 + |c_B|^2 = 1$. The relative magnitude of the coefficients c_A and c_B can be taken as a measure of the polarization (covalent character) of the bond. For a perfectly covalent (apolar) bond, $|c_A|^2 = |c_B|^2 = 1/2$. In this work, we use the square of the coefficient of the hybrid on the central carbon as a measure of the covalency of the Fe—C bond.

INTRODUCTION

E0 State of WT, α-Ile70, and α-Ala70 MoFe Proteins.

The FeMo-cofactor in the resting state E_0 of the WT protein and its variants has a true electron spin, $S = 3/2$, but its EPR spectrum is commonly discussed in terms of a fictitious spin, $S' = 1/2$, and described by an effective g-tensor characterized by g-values, $\boldsymbol{g}' = [g_1', g_2', g_{\parallel}] = [4.30, 3.67, 2.01]$ for the WT enzyme (Table 1),[1,56,57] with an orientation relative to the FeMo-cofactor that has been determined by single-crystal EPR.[58] In our previous study, the complete ^{13}C carbon hyperfine tensor for the FeMo-cofactor in the WT protein E_0 state as expressed relative to the fictitious spin $S' = 1/2$, denoted $^{C}\boldsymbol{A}'$, was determined from analysis of the 2D pattern of ENDOR spectra collected across the EPR spectrum.[15] The simulation of this pattern gives the relative signs of the resulting hyperfine tensor components; the absolute sign was determined from the so-called "pseudo-nuclear Zeeman" shift of the apparent ^{13}C Larmor frequency.[59] The three tensor elements, $^{C}\boldsymbol{A}' = [A_1', A_2', A_3']$, thus determined are related to those for the ^{13}C carbon hyperfine tensor relative to the E_0 true spin 3/2, hyperfine tensor, $^{C}\boldsymbol{A}$ (Table 1) with near-zero isotropic coupling, $^{C}a = +0.86$ MHz, nearly identical in magnitude but opposite in sign to the coupling observed at the high-field edge of the EPR spectrum, $g = 2.035$, $A_3 = -0.88$ MHz (see below).

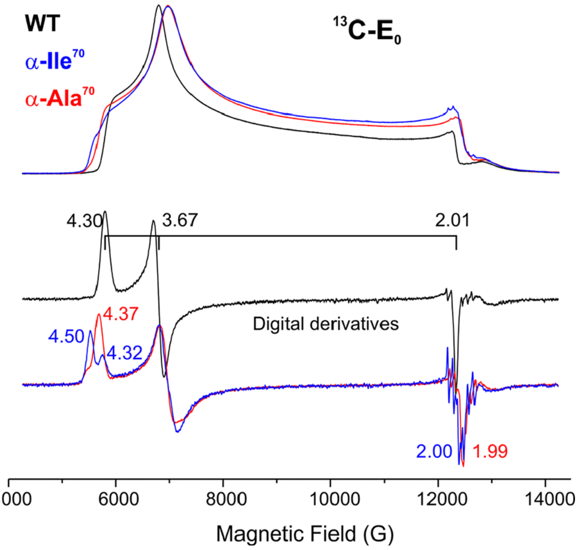

Figure 2. CW, absorption-display rapid passage $T = 2$ K EPR spectra and digital derivatives taken for resting state nitrogenase WT (black), α-Ile^{70} (blue), and α-Ala^{70} (red) MoFe proteins prepared with targeted ^{13}C labeling; spectra normalized in amplitude for comparison. Conditions: microwave frequency 34.696 GHz (WT), 34.727 GHz (α-Ile^{70}), and 34.879 GHz (α-Ala^{70}), microwave power 10 μW, modulation amplitude 1 G, time constant 128 ms, scan time 4 min.

The EPR spectrum of the FeMo-cofactor in the E_0 resting state of the α-Ile^{70} protein exhibits the previously reported difference from the WT protein spectrum.[22] While the WT protein E_0 EPR spectrum shows the presence of a single EPR-active state with effective g'-values given in Table 1, the EPR of the α-Ile^{70} protein (Figure 2) reveals the presence of two conformers, one similar to that of the WT protein and the other that is perturbed by an alternative positioning of the large side chain of the substituting Ile residue. The FeMo-cofactor in the WT-like conformer has g'-values of E_0 close to those in the E_0 state of the WT protein, indicating that that form of the FeMo-cofactor is negligibly perturbed compared to the WT protein. The other conformer demonstrates noticeably increased rhombicity [e.g., $g_1'(\alpha\text{-Ile}^{70}) = 4.50 > g_1'(\text{WT}) = 4.30$, Table 1] and less-resolved features at fields associated

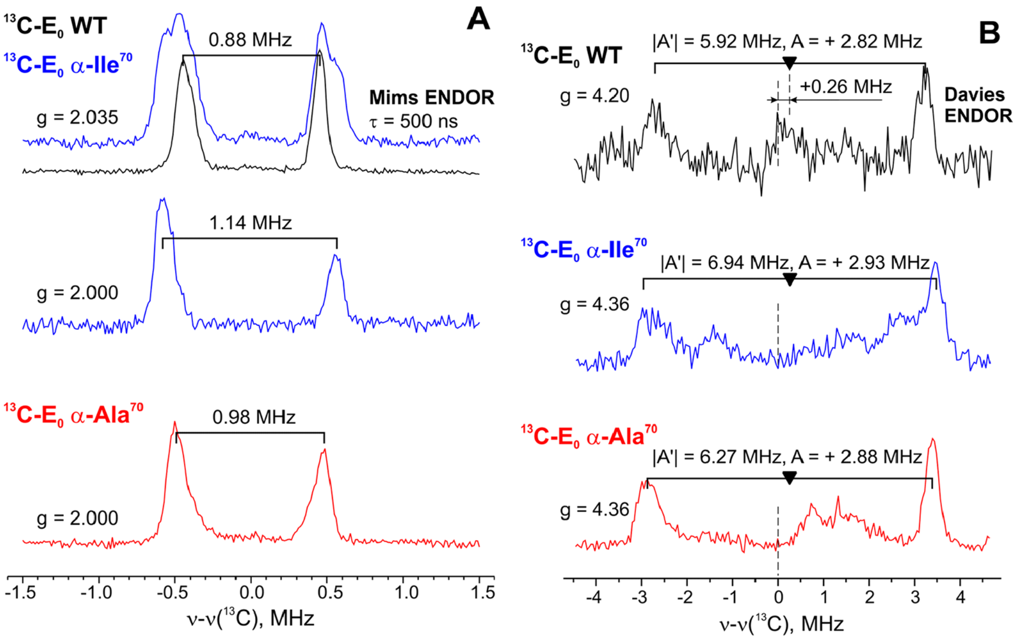

Figure 3. Pulse ENDOR spectra measured near g_3 (A) and g_1 (B) of resting-state nitrogenase WT (black), *α*-Ile^{70} (blue), and *α*-Ala^{70} (red) prepared with targeted ^{13}C labeling of the FeMo-cofactor. The values of the hyperfine splittings of the ^{13}C doublets are listed in the figure. Analysis of the offset of the doublets in (B) from the nuclear Larmor frequency for the $S = 3/2$ E_0 state, as illustrated for the WT protein, yields the positive sign of the ^{13}C coupling. Figure S1 presents spectra that show that additional small features in the spectra of (B) are background signals also present in samples without ^{13}C labeling; they are primarily signals from natural-abundance ^{95,97}Mo. Conditions: $T = 2$ K, Mims (A) and Davies (B), microwave frequency ∼ 34.65 GHz, $t(\pi/2) = 50$ ns (Mims) and 40 ns (Davies), $\tau = 500$ ns (Mims) and 600 ns (Davies), $T_{RF} = 40$ μs; repetition time 10 ms.

with the other components of the *g*-tensor. ^{95}Mo ENDOR of the isotopically enriched *α*-Ile^{70} protein was further found to exhibit distinct signals from the two conformers, with one conformer exhibiting the same isotropic hyperfine coupling as that of the WT protein but the other, perturbed, conformer exhibiting a noticeably increased coupling.[60] Measurements of zero-field splitting (ZFS) of the $S = 3/2$ states via use of the pseudo-nuclear Zeeman effect on the observed ^{95}Mo Larmor frequency further revealed a substantially decreased ZFS value for the perturbed conformer relative to that for the WT protein resting state.

The ^{13}C carbon ENDOR of the $S = 3/2$ E_0 state of the WT enzyme as reported earlier and spectra newly taken at g_1' and g_3' are shown in Figure 3. A shift of the ^{13}C doublet at $g1'$ away from the Larmor frequency, as shown for the WT protein in Figure 3B, is caused by the pseudo-nuclear Zeeman effect and yields a positive sign of the ^{13}C hyperfine coupling. In contrast to ^{95}Mo ENDOR, ^{13}C ENDOR of the *α*-Ile^{70} protein resting state prepared with targeted ^{13}C labeling of the cofactor showed only insignificant differences in the carbon hyperfine coupling in the two conformers of the substituted protein (Figure 3). Thus,slightly differing contributions of the two conformers can be detected at $g = 2.035$ as two resolved ^{13}C ENDOR doublets, and at $g = 2.00$, only the "perturbed" conformer contributes to the EPR and thus the ENDOR spectrum (Figure 3A). The "WT" conformer coupling is the same as that of ^{13}C carbon in the WT protein, $A_3 = -0.88$ MHz, confirming that the carbon of this conformer is spectroscopically indistinguishable from that of the WT protein itself, while the "perturbed" conformer exhibits a doublet splitting of only slightly larger magnitude, $A_3 = -1.14$ MHz. On the other hand, spectra taken at the low field edge of the EPR spectrum near g_1' revealed only a single ^{13}C ENDOR doublet (Figure 3B), indicating that at this field, the ^{13}C carbon couplings of the two conformers are indistinguishable. These observations can be linked to prior ^{95}Mo ENDOR measurements, which showed that the properties of this "capping" metal ion are similarly slightly altered by the subtle conformational changes induced by the substitution.

Whereas substitution of the *α*-Val^{70} residue present in the WT MoFe protein by the bulkier *α*-Ile^{70} residue hinders the binding/reduction of all substrates except protons, substitution by *α*-Ala^{70} opens the binding site to accommodate binding/reduction of larger substrates such as PA. Unlike the situation with the *α*-Ile^{70} protein, the EPR spectrum of the FeMo-cofactor in the resting state of the *α*-Ala^{70} protein shows a signal from only one cofactor conformation, with $g' = [4.37, 3.60, 1.99]$, which is not very different from FeMo-cofactor in the WT protein (Figure 2). ENDOR spectra measured at the edges of the *α*-Ala^{70} protein EPR envelope revealed $A_1 = +2.88$ MHz and $A_3 = -0.98$ MHz, values that differ minimally from those of the FeMo-cofactor carbon within the WT protein (Figure 3). Thus,structural perturbations of the FeMo-cofactor in the E_0 state induced by amino acid substitutions are readily observed by EPR as differences in *g*-values and by ^{95}Mo ENDOR, but the carbon is largely oblivious to such perturbations, as measured by ^{C}a.

Turnover Intermediates of WT, *α*-Ile^{70}, and *α*-Ala^{70} MoFe Proteins. All four of the turnover intermediates studied here are low-spin, $S = 1/2$ with similar near-axial *g*-tensors, $g_1 = g_\parallel > g_2 \sim g_3$, with $g_\parallel \sim 2.1$ and $g_\perp = (g_2 + g_3)/2 \leq 2$ for all but hi-CO (Figure 4 and Table 1). Examining the ^{13}C ENDOR of their central carbon tests for distortions of the FeMo-cofactor that has been activated through accumulation of reducing equivalents and the binding of exogenous ligands to Fe, and thereby offers insights into the role of the central carbon.

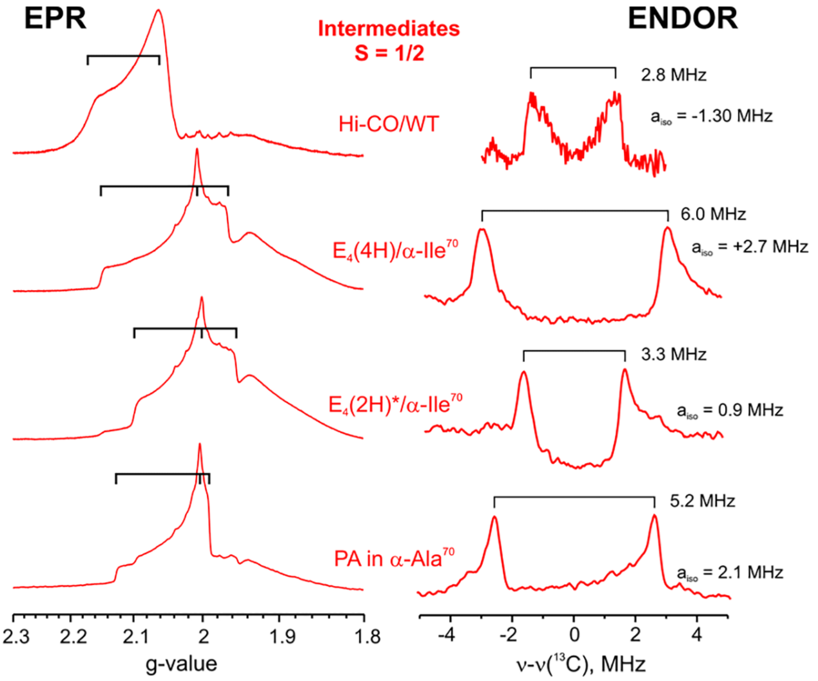

Figure 4. (Left) CW, absorption-display rapid passage $T = 2$ K EPR spectra. (Right) ^{13}C ENDOR spectra taken at $g_{||}$ for various $S = 1/2$ turnover intermediates trapped in WT and substituted MoFe proteins that had undergone targeted ^{13}C labeling of the FeMo-cofactor. Conditions: EPR, microwave frequency 34.823 GHz (hi-CO), 34.816 GHz [E_4(4H) and E_4(2H)*], and 34.778 GHz (PA), microwave power 10 μW, modulation amplitude 1 G, time constant 128 ms, scan time 4 min; ENDOR, conditions, see Figure 5.

Figure 4 also shows ^{13}C carbon ENDOR spectra for each of these states collected at their respective $g_{||}$. The couplings are noticeably larger than those at $g_{||}$ for the resting-state FeMo-cofactor and vary among themselves, but as we now show, the isotropic couplings in fact are only modestly changed. Characterization of the ^{13}C carbon hyperfine tensor for each state generated under turnover conditions is described below.

Hi-CO. The hi-CO state is an inhibited "dead end" state formed during turnover of the WT protein under high CO pressure.[19,61] We recall the recently reported results of ^{13}C carbon ENDOR on this state[15] as a benchmark for the study of the other intermediates.

The hi-CO g-tensor is axial, with $g_{||} = 2.17$ and $g_{\perp} = 2.06$. As shown in Figure 5A, the breadths of the ^{13}C ENDOR spectra at the low- and high-field edges of the spectra are comparable, as one might expect for a near-isotropic hyperfine tensor. However, the breadth decreases toward the middle of the 2D pattern, which is shown by simulations to require a highly anisotropic tensor, with hyperfine tensor components of differing signs. Through the use of the PEST RE protocol[62] to determine the absolute signs, the simulations show that $^{C}\boldsymbol{A}$ = [+3.2, −3.4, −3.7] MHz, and the isotropic coupling thus is not significantly greater than that of E_0, $^{C}a = -1.3$ MHz (Table 1).

E_4(4H) Intermediate. During turnover under Ar, the resting state E_0 of the α-Ile^{70} protein is lost in favor of a reduced state that appears in the EPR spectrum as an $S = 1/2$ signal with g-tensor $\boldsymbol{g}$ = [2.150, 2.007, and 1.965]. The previous ENDOR spectroscopy indicated that this signal arises from the E_4(4H) state in which the four e$^-$/H$^+$ accumulated by the cofactor are present as two [Fe−H−Fe] bridging hydrides, one Fe2−H−Fe6 bridge and the other Fe3−H−Fe7.[22,24] This is the central intermediate in the catalytic cycle, activated for binding/reduction of N_2 coupled with the release of H_2.[32]

Various possibilities have been considered about additional details of this di-hydride bound state, including whether S2B, which bridges Fe2−Fe6 in the resting state, retains both bonds to Fe and is protonated, has had the Fe2 bond broken, and is present as a sulfhydryl bound to Fe6, or even is lost as SH$^-$.[30,51,63,64]

Figure 5B shows the 2D field-frequency pattern of ^{13}C ENDOR obtained across the EPR envelope of the E_4(4H) state trapped during turnover of the α-Ile^{70} protein prepared with targeted ^{13}C labeling of the FeMo-cofactor. The spectrum at g_1 exhibits a sharp ^{13}C doublet with hyperfine coupling corresponding to $A_1 \sim 6$ MHz. With increasing field (decreasing g-value), the splitting decreases with noticeable broadening and splitting of the signals, characteristics that are in part obscured by distortions caused by slow relaxation. Overall, the pattern suggests that the largest hyperfine component is associated with g_1 and that the g_2 and g_3 components are significantly smaller. The hyperfine splitting at g_3 is also well defined, indicating $A_3 \sim 2$ MHz, but the spectra in the vicinity of g_2 are sufficiently distorted by sweep artifacts that any direct estimate of A_2 from this data is not persuasive.

Detailed investigation with pulse Mims ENDOR clarified the uncertainties introduced by the sweep distortions of the E_4(4H) CW ENDOR pattern near the ^{13}C Larmor frequency, Figure 6. The field dependence of Mims ENDOR taken near the g_2 maximum of the EPR signal shows that the ENDOR response rises to a maximum at g_2, rather than exhibiting a null as suggested by the CW spectra (Figure 6A). Although the Mims spectra appear to show a doublet of very small splitting, the absence of intensity at the Larmor frequency is introduced by a null in the Mims response function at the Larmor frequency (see Materials and Methods). Thus, what appears to be an intense doublet instead is the signature of a maximum at

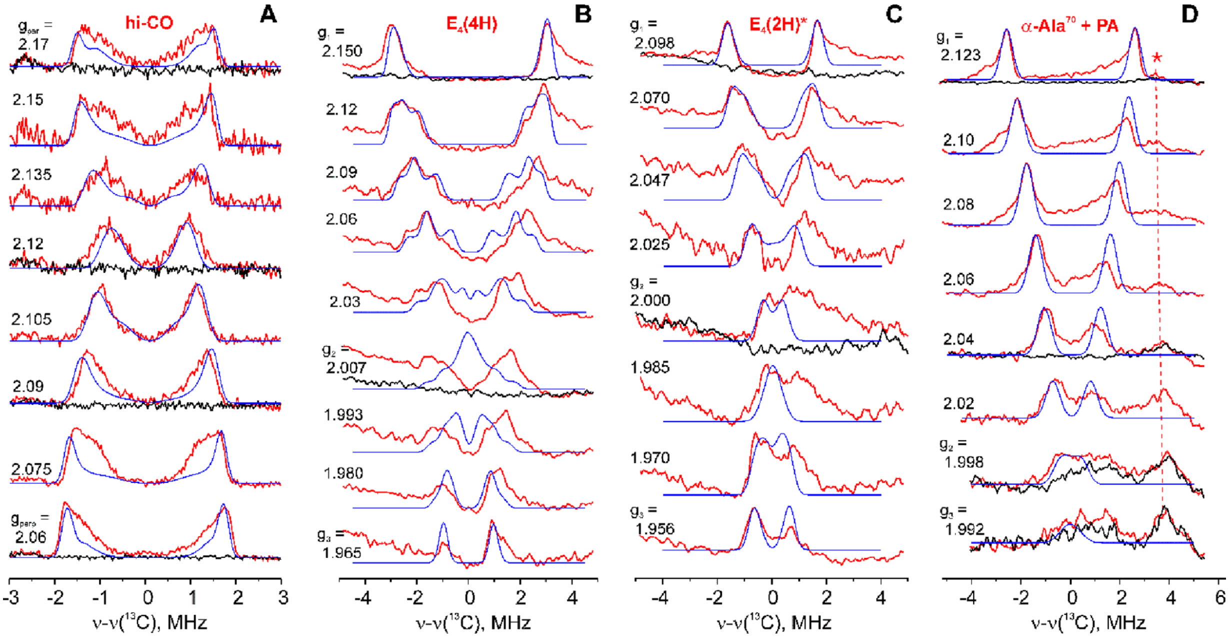

Figure 5. (A) **hi-CO**. 2D field/frequency patterns of 35 GHz ReMims pulsed ENDOR spectra of FeMo-cofactor in the hi-CO state: (red) with targeted ^{13}C labeling; (black) natural abundance; (blue) simulations that take into account distortions described in Materials and Methods. Direct simulation of this 2D pattern for the $S = 1/2$ state yields $^{C}\boldsymbol{A}$ = [+3.2, −3.4, −3.7] MHz, with rotation angles α = 0°, β = 5°, and γ = 15°. Conditions: T = 2 K, ReMims, microwave frequency ∼ 34.72 GHz, $t(\pi/2)$ = 30 ns, τ_1 = 140 ns, T_{RF} = 40 μs, repetition time 50 ms. (B) **E_4(4H)**. CW T = 2 K ^{13}C ENDOR spectra of the E_4(4H) state of the α-Ile^{70} MoFe protein prepared with (red) and without (black) targeted ^{13}C labeling of the FeMo-cofactor. Blue traces are simulations obtained with the following parameters: $^{C}\boldsymbol{A}$ = [+6.3, 0, +1.9] MHz, rotation angles α = 10°, β = 10°, and γ = 0°. Conditions: microwave frequency 34.82 GHz, microwave power 0.3 μW, modulation amplitude 2.5 G, low−high-frequency RF scan, RF sweep speed 1 MHz/s, time constant, 64 ms; RF bandwidth-broadened to 100 kHz. (C) **E_4(2H)***. CW T = 2 K ^{13}C ENDOR spectra of the E_4(2H)* state photo-induced in the α-Ile^{70} protein prepared with (red) and without (black) targeted ^{13}C labeling. Blue traces are simulations obtained with the following parameters: $^{C}\boldsymbol{A}$ = [3.6, 0.8, −1.6] MHz, with rotation angles α = 5°, β = 10°, and γ = 0°. Conditions: microwave frequency 34.82 GHz, microwave power 0.3 μW, modulation amplitude 2.5 G, low−high-frequency RF scan, RF sweep speed 1 MHz/s, time constant, 64 ms; RF bandwidth-broaden to 100 kHz. (D) **α-Ala^{70}+ PA**. CW T = 2 K ^{13}C ENDOR spectra of the PA intermediate state trapped during turnover of the α-Ala^{70} protein with PA prepared with (red) and without (black) targeted ^{13}C labeling of the FeMo-cofactor. The dashed red line (*) shows the position of ^{1}H harmonics. The ^{13}C carbon signal decreases in intensity with a decreasing g-value. For clarity, the spectra are normalized to the same amplitude; as a result, background signals, particularly the ^{1}H harmonics, appear to increase in relative intensity in the normalized spectra as the g-value decreases. Blue traces are spectra simulated using the following parameters: $^{C}\boldsymbol{A}$ = [5.5, 1.3, 0] MHz, with rotation angles α = 0°, β = 0°, and γ = 0°. Conditions: microwave frequency 34.78 GHz, microwave power 0.1 μW, modulation amplitude 2.5 G, high−low-frequency RF scan, RF sweep speed 1 MHz/s, time constant 64 ms; RF bandwidth-broadened to 100 kHz.

the ^{13}C Larmor frequency in the intensity of the ENDOR pattern determined by the "statistical" summation of centers differently aligned with the magnetic field; the Mims response creates the hole at the Larmor frequency.[40] Furthermore, the appearance of an ENDOR signal in this area is not an indication of the hyperfine coupling sign change seen for hi-CO, as simulations demonstrate that the ^{13}C ENDOR spectrum of E_4(4H) would collapse into a single central line at g_2 of this rhombic g-tensor, whereas the experiment shows a broad pattern with signals with splitting ranging up to ∼3.5 MHz. The field dependence spectra can be well simulated with a hyperfine tensor that has components of the same signs, but with one vanishingly small component: $^{C}\boldsymbol{A}$ = [+6.3, 0, +1.9] MHz, with ^{C}a = +2.7 MHz and anisotropic contribution $^{C}\boldsymbol{T}$ = [+3.6, −2.7, −0.8] MHz. Simulations of the Mims spectra that incorporate this hyperfine interaction and which include the effects of the tau-dependent "holes" in the Mims response function, $I(A) \sim 1 - \cos(2\pi A\tau)$, accurately reproduce the structure seen in the vicinity of the Larmor frequency, Figure 6B. The absolute sign of the hyperfine couplings was attained by a PESTRE measurement at g_1 (see Supporting Information, Figure S2).

E_4(2H)* State. Upon irradiation of the α-Ile^{70} protein captured in the E_4(4H) state with 450 nm light at cryogenic temperatures, the two bridging hydrides (Scheme 1) liberate H_2 via reductive elimination, leaving the cofactor in a state with the metal core reduced by two electrons and two protonated sulfurs.[25,33] The state has been designated as E_4(2H)* (Scheme 1), and it appears in the EPR spectrum of the irradiated sample as a signal with g = [2.098, 2.000, 1.956] (Figures 4 and S3). The state, which does not accumulate during turnover of the WT protein, is converted back to E_4(4H) by oxidative addition of H_2 in the frozen solution at temperatures higher than 175 K. ENDOR spectroscopy of E_4(2H)* for a protein enriched with ^{57}Fe or ^{95}Mo revealed that the two electrons remaining after reductive elimination of two hydrides were located on irons, likely to those coordinated to the carbon that had bridging hydrides in the E_4(4H) state.[14] Therefore, it was to be expected that the ^{13}C hyperfine coupling of the central carbon would change dramatically in the E_4(2H)* state. Instead, the ^{13}C ENDOR spectra of E_4(2H)* exhibit a field-frequency pattern different from that of E_4(4H) but without significant change in the range of carbon hyperfine coupling, Figure 5C. The ^{13}C carbon hyperfine splitting for E_4(2H)* is noticeably smaller at g_1 than for the

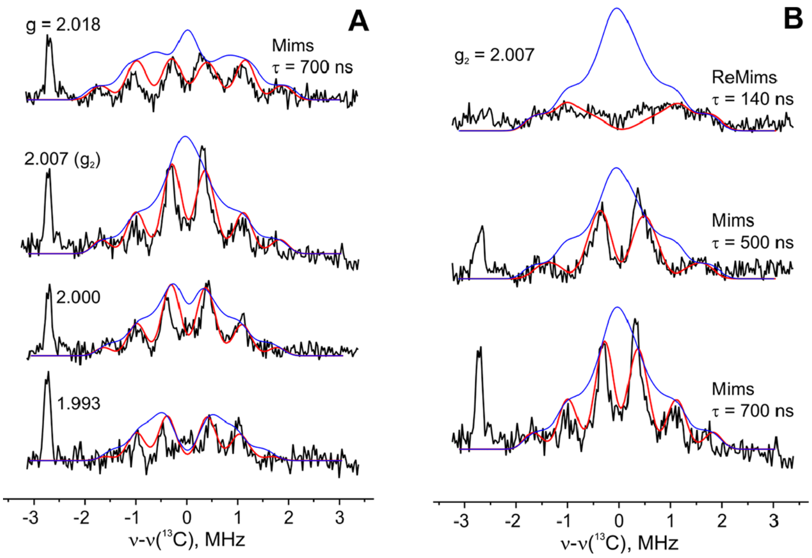

Figure 6. Pulse ^{13}C ENDOR spectra of the E_4(4H) state in the α-Ile^{70} protein with ^{13}C-targeted labeling taken with the g-value varied near g_2 (A, Mims with τ = 700 ns) and with varied τ parameter of the ENDOR sequence at g_2 (B). Mims and ReMims spectra normalized to the same spin echo for comparison. The thin traces represent simulations of ENDOR spectra, (red) considering distortions induced by "blind spots" of Mims sequence and (blue) without doing so; parameters of simulations are the same as in Figure 5B. The sharp signals near $\nu - \nu(^{13}C) \sim -2.75$ MHz arise from ^{1}H harmonics. Conditions: T = 2 K, microwave frequency ~ 34.63 GHz, $t(\pi/2)$ = 50 ns (30 ns for ReMims), T_{RF} = 40 μs, repetition time 25 ms.

dihydride state, and with increasing magnetic field, the coupling decreases, collapsing near g_2. The relaxation effects discussed in Materials and Methods distort the ENDOR response near g_2, but a sharp signal at the ^{13}C Larmor frequency at this g-value can be detected with certainty, and the field dependence spectra can be well interpreted as resulting from a hyperfine tensor with a negligible value for A_2 and differing signs of the components: $^{C}\boldsymbol{A}$ = [3.6, 0.8, −1.6] MHz, $|^{C}a|$ = 0.9 MHz, $^{C}\boldsymbol{T}$ = [+2.7, −0.1, −2.5] MHz. It was not possible to determine the absolute sign of the hyperfine coupling for E_4(2H)* with PESTRE, and thus, only the relative signs of the ^{13}C carbon hyperfine tensor components and the absolute magnitude of ^{C}a are known. It was surprising that the ^{13}C carbon tensor in the E_4(2H)* state is very close to the tensor of the E_0 resting state, in both the magnitude of ^{C}a and the symmetry of the anisotropic contribution, although the metal core of these cofactor states is of a different spin and redox level. In other words, the carbon senses the same surrounding in these two states, regardless.

PA Intermediate. The EPR spectrum of the α-Ala^{70} protein trapped during turnover in the presence of PA (Figure 4) shows a strong S = 1/2 signal from an intermediate with an almost axial g-tensor [2.127, 2.004, 1.991], with the very low presence of the resting state E_0. Characterization by ENDOR indicated that the intermediate state is the allyl alcohol product of PA reduction, coordinated at Fe6 in a ferracycle binding mode, Scheme 1.[26] Thus, the state represents the final stage of reaction, with the reduction product bound to the FeMo-cofactor prior to its release. This state is of particular interest as theoretical work predicted enhancement of the central carbon coupling in comparison with the resting state by at least 1 order of magnitude for ligand binding at only one of the six irons surrounding it.[65]

ENDOR spectra of the α-Ala^{70} PA turnover state prepared with ^{13}C-targeted labeling of the FeMo-cofactor carbon showed a doublet with a hyperfine splitting of ~5 MHz at g_1 (Figures 4 and 5D). With increasing magnetic field, the splitting decreases without significant broadening of the peaks and essentially vanishes near g_3. As a result, the intensity of the ^{13}C signal decreases in parallel, even though the EPR intensity increases as the ENDOR field is traversed over the EPR spectrum from g_1 to g_2/g_3 (Figure 4). The simulation of the measured 2D pattern of ENDOR spectra (Figure 5D) yields the magnitudes and relative signs of the ^{13}C carbon hyperfine tensor components, but it was not possible to determine the absolute signs with PESTRE: $^{C}\boldsymbol{A}$ = [5.5, 1.3, 0] MHz, $|^{C}a|$ = 2.3 MHz, $^{C}\boldsymbol{T}$ = [+3.2, −1.0, −2.3] MHz. Thus, although the ENDOR field-dependence pattern appears different from those of both E_4(4H) and E_4(2H)* states, the ^{13}C hyperfine values, and in particular the isotropic couplings for the four trapped intermediates, are not significantly different (Table 1). Interestingly, early DFT computations suggested that ^{C}a would be ~10-fold greater for a ^{13}C carbon in the PA intermediate, with its bound allyl alcohol ferracycle involving Fe6 (Scheme 1) than for the E_0 resting state,[65] contrary to the experiment.

To put into perspective the similarities in the values of ^{C}a for all the nitrogenase states studied here, we first note that the signs of ^{C}a for two of the intermediates examined have been determined while those for the other two have not (Table 1). Nonetheless, it is possible to determine an upper bound to the spread in signed values for the intermediates. Considering the four possible choices of sign for those two without signs, the average value of ^{C}a for the four intermediates, denoted $^{C}a_{av}$, must fall in the range $-0.4 \leq {}^{C}a_{av} \leq +1.1$ MHz. This may be compared to the value for the WT protein E_0 state, $^{C}a \sim +0.9$ MHz.

Origin of the ^{13}C-Carbon Hyperfine Coupling. To understand the implications of the above measurements for bonding in the CFe$_6$ FeMo-cofactor core and for cofactor spin-coupling schemes, we first develop an analytical approach to understanding the carbon hyperfine couplings and their dependence on these schemes and then illuminate this with DFT computations.

Hyperfine Coupling of the ^{13}C Carbon to the Spin-Coupled FeMo-Cofactor Metal–Ion Framework. The ^{13}C carbon is covalently bonded to six "belt" high-spin Fe ions (Figure 1), but the magnitudes of the contributions from these Fe ions are not simply additive: the contribution to the ^{13}C carbon hyperfine coupling tensor, $^{C}\boldsymbol{A}$, from each Fe ion carries a sign and magnitude imposed by weighting factors (vector-coupling coefficients) associated with the scheme that describes the exchange-coupling among the metal ions of the FeMo-cofactor. The experimentally observed ^{13}C hyperfine coupling tensor for the carbon is the sum of a scalar isotropic coupling term and anisotropic coupling tensor, $^{C}\boldsymbol{A} = {}^{C}a\cdot\mathbf{1} + {}^{C}\boldsymbol{T}$. Building on previous treatments of a nuclear spin hyperfine-coupled to the electron spins of one or more metal ions within the exchange-coupled FeMo-cofactor multinuclear cluster,[66] the observed coupling tensor $^{C}\boldsymbol{A}$ can be written as the sum of weighted contributions from each of the six bonded "belt" Fe ions, eqs 1A, 1B and 1C, with each contribution being defined for the Fe-ion in the absence of exchange coupling to the other metal ions[14]

$$^{C}\boldsymbol{A} \equiv \sum_{i=2}^{7} K_i \cdot {}^{C}\boldsymbol{A}_{\boldsymbol{i}}^{\mathbf{un}} \tag{1A}$$

$$\sum_{M_i}^{8} K_i = 1 \tag{1B}$$

$$^{C}\boldsymbol{A}_{\boldsymbol{i}}^{\mathbf{un}} = {}^{C}a_i^{\mathrm{un}}\cdot\boldsymbol{1} + {}^{C}\boldsymbol{T}_{\boldsymbol{i}}^{\mathbf{un}}$$

and with each being the sum of an isotropic coupling term and anisotropic coupling tensor, $^{C}\boldsymbol{A}_i^{\mathbf{un}} = {}^{C}a_i^{\mathrm{un}}\cdot 1 + {}^{C}\boldsymbol{T}_i^{\mathbf{un}}$. In the summation eqs 1A, 1B and 1C defining $^{C}\boldsymbol{A}$, each $^{C}\boldsymbol{A}_i^{\mathbf{un}}$ is weighted by the dimensionless vector-coupling coefficients, K_i, which are the projections of the metal ion's local electron-spin onto the total cluster spin and whose sum over the eight spin-coupled cluster metal ions (M) is normalized to unity (eq 1B). ^{57}Fe and ^{95}Mo ENDOR measurements are used to determine the K_i.[13,14,41] ^{95}Mo measurements allow us to omit from the normalization sum in eqs 1A, 1B, and 1C the in-principle contribution of the Mo site because we have found the vector-coupling coefficient for Mo in each of the spin-coupled FeMo-cofactor states studied to date to be very small, which implies that the local Mo electron-spin is essentially orthogonal to the total cluster spin.[14,60] This leads to an operational normalization for the K_i as the sum of the seven Fe ions

$$\sum_{\mathrm{Fe}_i,\, i=1}^{7} K_i = 1 \tag{1C}$$

Isotropic Coupling to ^{13}C. We first focus on the isotropic ^{13}C coupling component, ^{C}a, which arises from spin density in the carbon s-orbital and thus is the most direct indicator of Fe–C covalency. According to eq 1A, this coupling is the sum of the K_i-weighted isotropic contributions, $^{C}a_i^{\mathrm{un}}$, to the $^{C}\boldsymbol{A}_i^{\mathbf{un}}$ from each of the six belt Fe ions, Fe(2–7), eq 2A. For illustrative purposes, we extend an averaging-approach introduced by Mouesca and co-workers (see ref 66 and recapitulated in the Supporting Information) by "symmetriz-ing" the six Fe$_i$–C bonds of these Fe ions through the assumption that each induces the same local (uncoupled) contribution to the isotropic ^{13}C coupling, namely, assuming, ${}^{C}a_i^{un} \to {}^{C}a^{un}_{avg}$. Incorporation of ${}^{C}a^{un}_{avg}$ into eq 1A yields the second, illuminating expression for the isotropic ^{13}C hyperfine coupling of eq 2A

$$\begin{aligned} {}^{C}a &\equiv \sum_{i=2}^{7} K_i \cdot {}^{C}a_i^{\mathrm{un}} \Rightarrow \left(\sum_{i=2}^{7} K_i\right) \cdot {}^{C}a_{\mathrm{avg}}^{\mathrm{un}} \\ &= (1 - K_1)\cdot {}^{C}a_{\mathrm{avg}}^{\mathrm{un}} \end{aligned} \tag{2A}$$

$$\begin{aligned} &K_1 \to +1 \Rightarrow \sum_{i=2}^{7} K_i \to 0 \\ &\Rightarrow {}^{C}a \to 0 \end{aligned} \tag{2B}$$

Equations 2A and 2B demonstrate that the normalization condition on the vector-coupling coefficients for the seven Fe ions, eq 1C, causes the contributions to the ^{13}C carbon isotropic hyperfine coupling from the "up ($K_i > 0$)" and "down ($K_i < 0$)" Fe spins of the six Fe ions bonded to the carbon to strongly cancel when the seventh Fe, Fe1, which is not bonded to the carbon, has large positive K_1, thus making the sum of the vector-coupling coefficients of the six approach zero (eq 2B). Deviations from $^{C}a = 0$ could imply that the null limit is approached but not fully reached and/or there is a difference between the average of ${}^{C}a^{un}{}_i$ for the three (↑) and the three (↓) Fe ions in the (3↑/3↓) FeMo-cofactor belt of six Fe ions. DFT computations presented below address this issue.

Considering first E_0, as noted above, previous DFT computations and ^{57}Fe ENDOR measurements have suggested that exchange-coupling among the full complement of the FeMo-cofactor metal ions in E_0 favors a ground state with the so-called "BS7" exchange-coupling scheme, in which the terminal Fe1 ion is "spin-up (↑)", namely, with $K_i > 0$, three of the six "belt" Fe ions bonded to the carbon also are "spin-up (↑)" and three are "spin-down (↓)", namely, $K_i < 0$, schematically denoted (3↑/3↓).[18,65] As illustrated in Figure 1C, in this scheme, the belt spins are arranged in antiferromagnetically coupled (↑/↓) pairs at the edges of the trigonal prism of Fe ions. Indeed, recent ^{57}Fe ENDOR measurements of WT resting-state E_0 in which Fe1 is selectively ^{57}Fe-labeled definitively yield a ^{57}Fe1 hyperfine coupling constant that in fact corresponds to the vector-coupling coefficient, $K_1 \sim +1$.[67] According to eqs 2A and 2B, this experimentally determined value $K_1 \sim +1$ then implies that the opposing contributions to ^{C}a from the BS7 spin-up and spin-down Fe ions of (3↑/3↓) CFe$_6$ essentially cancel.

Anisotropic Hyperfine and Zero-Field Splitting Tensors. The symmetrization approach can be used to discuss $^{C}\boldsymbol{T}$, the anisotropic contribution to $^{C}\boldsymbol{A}$, by assigning the same tensor components to the anisotropic contribution $^{C}\boldsymbol{T}_{\mathbf{avg}}^{\mathbf{un}}$ for each of the six belt Fe ions, Fe(2–7) in eqs 1A, 1B, and 1C. However, as noted in our earlier report,[15] because these local tensors are non-colinear, unlike the isotropic coupling, their summation as weighted by the K_i for the CFe$_6$ fragment does not cancel, even in the exact null limit on the K_i. As shown in the Supporting Information, this approach holds promise for helping to distinguish among the lowest-lying, nearly degenerate BS7-like spin-coupling configurations. The Supporting Information furthermore shows that its application to the ZFS interaction helps explain the intriguing report that the orientations of $^{C}\boldsymbol{T}$, and thus $^{C}\boldsymbol{A}$, are correlated with the orientation of the ZFS tensor, namely, that the unique axis of

Scheme 2. Visualization of the Alternative Consequences of Large and Small per-Bond Fe → C Spin Transfer on the Influences of a Hemilabile Fe−C Bond during Substrate Binding That Perturbs an Fe−C Bond; Left: Large Spin Transfer in the Bond Would Cause a Large Change in ^{C}a; Right: the Small Observed Changes in ^{C}a Are Compatible with Changing a Bond with Small Spin Transfer

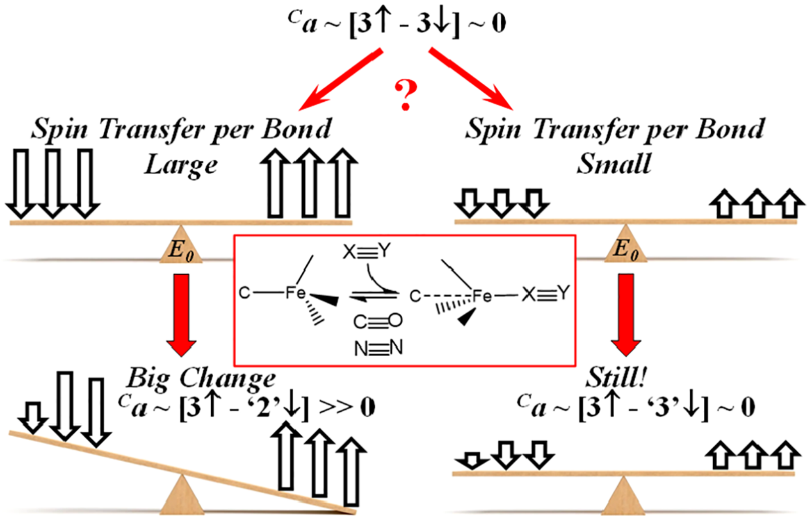

the ^{13}C carbon hyperfine tensor, A_3, is parallel to g_3, which lies along the unique axis of the ZFS tensor.

Spin Cancellation Alternatives. Each of the intermediates we have studied has a comparable carbon isotropic ^{13}C coupling—differing in magnitude by at most a few MHz from the small coupling in E_0. To reach an understanding of these observations in terms of the spin-coupling schemes and Fe−C bonding in the intermediates requires an understanding of the magnitude of the $^{C}a_i^{un}$, which in turn requires an under-standing of the Fe → C spin transfer in each of the Fe−C bonds. As visualized through the cartoon of Scheme 2, left, if spin-transfer per bond, and thus the resulting $^{C}a_i^{un}$, is large, then a BS7-like exchange-coupling scheme with a (3↑/3↓) arrangement of the Fe spins of the CFe$_6$ core[18,65] is required for each of the intermediates to explain the persistence of a small magnitude for ^{C}a, comparable to that observed for E_0. In this case, a transformation that involves weakening of/breaking an Fe−C bond(s) would drop the spin-transfer in that bond so as to annul the cancellation, even with a (3↑/3↓) spin-coupling scheme, creating a large net spin on C and thus a large ^{C}a, with magnitude on the order of that associated with the spin contribution in that bond. Correspondingly, a change in the spin coupling would do likewise.

Thus, if spin transfer in the Fe−C bonds is large, the experimental cancellation of spin density at carbon in intermediates implies that in every state we have examined, the FeMo-cofactor retains both a BS7-type (3↑/3↓) spin-exchange coupling scheme and an essentially unperturbed CFe$_6$ core.

However, if spin-transfer per bond is small, then a large percentage-change in spin transfer in one bond caused by weakening of/breaking that bond, as shown in Scheme 2, right, or by a change in spin-coupling scheme would not cause a large change in ^{C}a, and thus, the experimental results would not rule out hemilabile changes in Fe−C bonding and geometric structure of the CFe$_6$ core.

We next present DFT computations that show spin-transfer per bond is indeed large in every state we have examined, and therefore in each of these states, the FeMo-cofactor has a BS7-type spin-exchange coupling scheme, with resulting cancellation of the large spin density contributions to carbon from the (3↑/3↓) Fe ions in an essentially structurally invariant CFe$_6$ core.

DFT Computations Distinguish between Spin Cancellation Alternatives. As explained directly above and visualized in Scheme 2, knowledge of the magnitudes of the contributions from the individual Fe−C bonds to the net spin density on C is required to understand the significance of the observed small differences in ^{C}a among the states we have studied. To thus understand the electronic origin of the cancellation of the carbon isotropic hyperfine coupling, we carried out DFT computations to parallel the experiments and underpin eqs 1A, 1B, 1C, 2A, and 2B (see the Supporting Information). Specifically, we examined the structurally characterized E_0 and hi-CO states, the E_4(2H)* state,[33] the H_2-bound complex E_4(H_2,2H), which we proposed as an intermediate along the pathway to the formation of E_4(2H)*,[68] as well as revisiting our previous computations of the central state in nitrogen fixation, the E_4(4H) state.[41] The ground state of each case examined here shows a BS7-like (3↑/3↓) arrangement of the Fe spins of the CFe$_6$ core and a negligible computed total spin density on the central carbon (Table S1). This correspondence with the experiment validates the formulation of the hyperfine coupling in terms of the model eqs 1A, 1B, 1C, 2A, and 2B and leads us to utilize the DFT results to look more deeply into the per bond Fe → C spin transfer in ^{13}CFe$_6$. By showing whether the spin-transfer per bond is large or small, the DFT computations thereby explain the significance of the observed differences in ^{C}a among the states we have studied and resolve the dichotomy illustrated by Scheme 2.

To assess the Fe → C spin transfer in ^{13}CFe$_6$, we calculated the NBOs from Kohn−Sham wavefunctions for E_0, hi-CO, E_4(4H), E_4(2H)*, and E_4(H_2,2H). These orbitals allow a quantitative analysis of the bonding hybridization and covalency in terms of concepts similar to Lewis chemical structures.[29] In every state examined, we find the CFe$_6$ core features six comparable Fe−C NBOs, one for each of the bonded Fe sites, which involve the overlap between the Fe $3d_{z^2}$ natural atomic orbital and a C sp^2-like natural hybrid orbital; an example of such orbitals is shown in Figure 7a. The computations show that the CFe$_6$ Fe−C bonds are highly covalent, as indicated by the DFT electron density distribution in E_0 (as shown for the Fe2−C bond of E_0, Figure 7b) and quantified by a detailed NBO analysis. Each bond contains almost exactly one electron, ($\langle n \rangle \approx 1$, Table S1). These orbitals feature roughly equal electron sharing between Fe and C, with a small polarization toward C as expected from the difference in electronegativity of C and Fe. The average square of the coefficient of the sp^2-like hybrid on C is only slightly affected by the ligation state of the FeMo-cofactor, only ranging between $|c|^2 \approx 0.64$ for E_0 and 0.57 for Hi-CO (Table S1), with one-third of that associated with the carbon 2s orbital component of the sp^2-like orbital. Thus, given $\langle n \rangle \approx 1$, each orbital contributes ~0.2 spin in the carbon 2s, as illustrated in detail by the NBO-bond carbon 2s spin densities of Table S2.

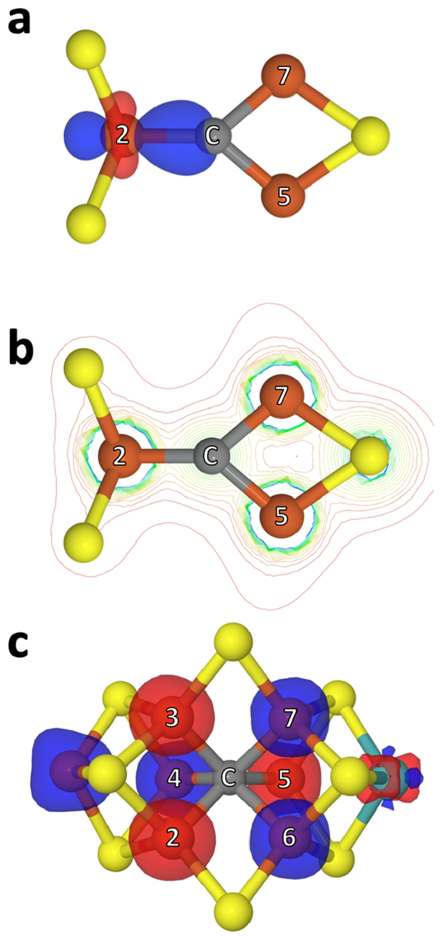

Figure 7. (a) Natural bond orbital for the Fe2−C covalent bond in E_0 and electron spin density. The orbital surface encloses 75% of the orbital electron density (about 0.75 e^-). (b) Total electron density of the E_0 FeMo-cofactor in the plane identified by Fe2, Fe5, and Fe7. The contour density lines are drawn from a density of 0.4 e/Å^3 (blue/green lines) to 0.01 e/Å^3 (outer red line). (c) Spin density over the FeMo-cofactor cluster (surfaces are plotted at ±0.14 e/Å^3 isodensity). Blue and red surfaces indicate negative and positive values of the orbital in (a) and of the spin density in (c). Fe atoms are shown in rust, the Mo atom in cyan, and S atoms in yellow. For the sake of visualization, in (a,b), only the FeMo-cofactor atoms close to the Fe2−Fe5−Fe7 plane are shown in balls and sticks.

Using the textbook value for the isotropic coupling for one electron in a carbon 2s orbital, $a_{2S} \approx 3800$ MHz,[16,17] the estimated 0.2e spin contribution per Fe−C bond to 2s of the central carbon results in an isotropic coupling contribution $|a| \sim 0.2\ a_{2S} = 760$ MHz per bond, with the sign determined by the vector-coupling coefficient for the Fe (K_i, eqs 1A, 1B, and 1C). The observed ^{13}C hyperfine coupling for every intermediate thus is indeed extremely small compared to the contribution from an individual bond. This must therefore occur because the (3↑/3↓) configuration of Fe$_6$ spins generates overall cancellation of the large individual contributions so as to give the small net spin on (Figure 7c), and isotropic coupling to, the central carbon as seen experimentally (Table 1). Put simply, the observed isotropic couplings for all states studied are the truly negligible differences of two huge numbers

$$
{}^{C}a \sim +3[\sim(760)] - 3[\sim 760)] \rightarrow [-1.3 \leftrightarrow +2.7]\,\text{MHz}
$$

$$
(\text{experiment}) \leftrightarrow \sim 0
$$

a result confirmed through consideration of an internal control provided by the couplings to the two ^{13}CO of hi-CO (see the Supporting Information). In turn, given the spin and hyperfine-coupling contributions to the interstitial carbon from each Fe−C bond is large (Scheme 2 left), the comparably small ^{C}a for the several E_0 states and intermediates then indicates that no intermediate can have an Fe−C bond that is appreciably weakened/altered upon its formation.

Structural Invariance. The near-equivalence of the six Fe−C bonds exhibited in their NBOs (e.g., Table S2) is paralleled in the nearly perfect trigonal prismatic geometry of the CFe$_6$ in all states investigated. This is best captured by the order parameter $O(D_{3h}) = 0$(see Materials and Methods), which measures the deviations of the CFe$_6$ core from the ideal D_{3h} symmetry. For each D_{3h} symmetry operation, each Fe atom is transformed to another. The operator measures the distance between each atom and the symmetry-related partner into which it transforms. This distance is averaged over all operations and all six belt Fe atoms. For ideal D_{3h} symmetry, $O(D_{3h}) = 0$; in all states studied, $O(D_{3h}) = 0 \leq 0.1$ Å, with comparable values for computed and crystallographic struc-tures (Table S1). Importantly, a comparable analysis shows that the carbon remains at the center of the CFe$_6$ trigonal prism in the structures for all states, with $O(D_{3h}) = 0 < 0.07$ Å for the C atom. The prismatic symmetry is further reflected by nearly uniform Fe−C bond lengths, with an average value of about 1.95 Å and typical standard deviations from the average of about 0.05 Å. In short, as observed crystallographically for WT E_0 and hi-CO[20] and found computationally for these and the other intermediates (Table S1), there occurs no statistically significant distortions from trigonal CFe$_6$ symmetry or change in Fe−C bond lengths, just as there is no significant change in the covalent Fe−C bonding/spin-delocalization in the CFe$_6$ core (Scheme 1).

In summary, major changes in spin state, charge, and ligation seen for the diverse intermediates do not alter either the CFe$_6$ geometry or the spin density on the core ^{13}C. All six Fe−C bonds contribute spin density of a comparably large magnitude to the carbon 2s orbital, which implies that the extremely small isotropic ^{13}C hyperfine coupling is the result of the cancellation of large contributions of opposite sign, thus demonstrating the persistence of the (3↑/3↓) exchange-coupling scheme seen in E_0. The profound implications of these findings for the role of the CFe_6 core in catalysis are summarized below.

Beyond this, it is of interest to note that while Table 1 shows that ^{C}a varies minimally among the states examined, the ^{13}C anisotropic coupling tensors nonetheless vary sharply in orientation and symmetry and appreciably in magnitude. This tensor reflects details of the BS7-type exchange-coupling scheme adopted by a state, and thus, the ^{13}C ENDOR gives an intimate probe of those schemes as well.

CONCLUSIONS

Despite the differences among the four turnover intermediates and inhibited states we have studied, differences in the spin state, the substrates/fragments bound to the cofactor and in their modes of binding to Fe ions of the cofactor, the geometry of the CFe_6 core of FeMo-cofactor in E_0 is retained in the intermediates, as shown by X-ray diffraction for hi-CO and found by DFT for other states (Table S1). Similarly, all exhibit an extremely small isotropic ^{13}C carbon hyperfine coupling (Table S1). In particular, it is surprising and suggestive that both the $S = 1/2$ hi-CO state, which has lost S^{2-} and binds two CO to belt Fe and thus is apparently the most "perturbed" relative to $S = 3/2$ E_0, and the intermediate $E_4(2H)^*$, which has no exogenous ligand bound to the doubly reduced metal ions, have a ^{13}C carbon tensor very close to that of the resting state, with similar magnitudes of ^{C}a and symmetries of the anisotropic contribution. In other words, the central carbon has the same net interaction with its surrounding Fe ions in the resting state as in both of these two quite differently liganded states and indeed in each of the four intermediates examined.

As visualized in Scheme 2, if the magnitude of spin density delocalized to carbon through an individual Fe−C bond were small, then the spin-density imbalance and associated carbon hyperfine could also be small for an intermediate, even if an Fe−C bond were hemilabile and weakened or broken. However, our DFT computations indicate that the individual contributions are not small, and thus, if such hemilability were operative in an intermediate, then ^{C}a would be large. However, the present results show that this is not the case. In each of the present, highly diverse, sampling of five different states (Scheme 1), ^{C}a remains small both experimentally and computationally, while the per bond Fe → C spin transfer is large (Scheme 3), and the trigonal prismatic geometry around the carbon is maintained with high precision.

Our findings thus reveal that for the diverse states so far examined, while the FeMo-cofactor CFe_6 core is not impervious to changes in state, which do have a small influence on the ^{13}C hyperfine couplings, this core does not provide a functionally dynamic, hemilabile "beating heart" with Fe−C bonds weakening or breaking to allow substrate or inhibitor binding. Instead, in structure and in Fe−C bonding, it is essentially unchanged by turnover-induced transformations, a "heart of steel" that stabilizes the structure of the FeMo-cofactor active site during nitrogenase catalysis. The diversity of the states studied further suggests that the central role of this core is to stabilize the FeMo-cofactor active site throughout the catalytic cycle. Instead, it would appear that Fe−S bond(s) may well play the dynamic role first imagined for Fe−C, as seen in hi-CO[20] and elsewhere (e.g., refs 30, 31, 41, and 69).

Scheme 3. Implication of a Small ^{C}a and Structurally Invariant CFe_6 Core in All Examined Intermediates, Given Large Fe → C Spin Transfer per Fe−C Bond as Found by DFT

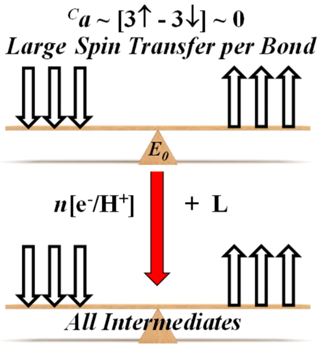

ASSOCIATED CONTENT

Supporting Information

The Supporting Information is available free of charge at https://pubs.acs.org/doi/10.1021/jacs.2c06149.

Additional EPR and ENDOR spectra, discussions of anisotropic ^{13}C hyperfine coupling and of zero-field splittings, CFe_6 electronic properties, NBO spin densities, and coordinates of computed species (PDF)

AUTHOR INFORMATION

Corresponding Authors

Simone Raugei − *Physical and Computational Sciences Directorate, Pacific Northwest National Laboratory, Richland, Washington 99352, United States;* orcid.org/0000-0001-9118-8480; Email: simone.raugei@pnnl.gov

Dennis R. Dean − *Biochemistry Department, Virginia Tech, Blacksburg, Virginia 24061, United States;* orcid.org/0000-0001-8960-6196; Email: deandr@vt.edu

Lance C. Seefeldt − *Department of Chemistry and Biochemistry, Utah State University, Logan, Utah 84322, United States;* orcid.org/0000-0002-6457-9504; Email: lance.seefeldt@usu.edu

Brian M. Hoffman − *Departments of Chemistry and Molecular Biosciences, Northwestern University, Evanston, Illinois 60208, United States;* orcid.org/0000-0002-3100-0746; Email: bmh@northwestern.edu

Authors

Dmitriy A. Lukoyanov − *Departments of Chemistry and Molecular Biosciences, Northwestern University, Evanston, Illinois 60208, United States;* orcid.org/0000-0002-4542-1648

Zhi-Yong Yang − *Department of Chemistry and Biochemistry, Utah State University, Logan, Utah 84322, United States;* orcid.org/0000-0001-8186-9450

Ana Pérez-González − *Biochemistry Department, Virginia Tech, Blacksburg, Virginia 24061, United States;* orcid.org/0000-0002-7724-9985

Complete contact information is available at: https://pubs.acs.org/10.1021/jacs.2c06149

Notes

The authors declare no competing financial interest.

ACKNOWLEDGMENTS

We thank Alvaro Salinero-Lanzarote for performing cell growth and grants from the U.S. Department of Energy (DOE), Office of Science, Office of Basic Energy Sciences supported genetic studies, protein production, trapping of states for study, and ENDOR spectroscopy (DE-SC0010687, DE-SC0010834, and DE-SC0019342 to L.C.S., D.R.D., and B.M.H.). Support for S.R. was provided by the U.S. DOE, Office of Science, Office of Basic Energy Sciences, Division of Chemical Sciences, Geosciences, and Biosciences. Computer time was provided by the National Energy Research Scientific Computing Center (NERSC), a U.S. DOE Office of Science User Facility operated by Lawrence Berkeley National Laboratory, and the Molecular Sciences Computing Facility (MSCF) in the Environmental Molecular Sciences Laboratory, a DOE User Facility located at the Pacific Northwest National Laboratory (PNNL). PNNL is operated by Battelle for the DOE under Contract number DE-AC05-76RL01830.

REFERENCES

(1) Burgess, B. K.; Lowe, D. J. Mechanism of Molybdenum Nitrogenase. *Chem. Rev.* **1996**, *96*, 2983−3012.

(2) Thorneley, R. N. F.; Lowe, D. J. Kinetics and Mechanism of the Nitrogenase Enzyme System. *Metal Ions Biol.* **1985**, *7*, 221−284.

(3) Wilson, P. E.; Nyborg, A. C.; Watt, G. D. Duplication and Extension of the Thorneley and Lowe Kinetic Model for Klebsiella Pneumoniae Nitrogenase Catalysis Using a Mathematica Software Platform. *Biophys. Chem.* **2001**, *91*, 281−304.

(4) Lukoyanov, D.; Yang, Z. Y.; Duval, S.; Danyal, K.; Dean, D. R.; Seefeldt, L. C.; Hoffman, B. M. A Confirmation of the Quench-Cryoannealing Relaxation Protocol for Identifying Reduction States of Freeze-Trapped Nitrogenase Intermediates. *Inorg. Chem.* **2014**, *53*, 3688−3693.

(5) Lukoyanov, D. A.; Khadka, N.; Yang, Z. Y.; Dean, D. R.; Seefeldt, L. C.; Hoffman, B. M. Hydride Conformers of the Nitrogenase FeMo-Cofactor Two-Electron Reduced State E_2(2H), Assigned Using Cryogenic Intra Electron Paramagnetic Resonance Cavity Photolysis. *Inorg. Chem.* **2018**, *57*, 6847−6852.

(6) Seefeldt, L. C.; Yang, Z. Y.; Lukoyanov, D. A.; Harris, D. F.; Dean, D. R.; Raugei, S.; Hoffman, B. M. Reduction of Substrates by Nitrogenases. *Chem. Rev.* **2020**, *120*, 5082−5106.

(7) Spatzal, T.; Aksoyoglu, M.; Zhang, L. M.; Andrade, S. L. A.; Schleicher, E.; Weber, S.; Rees, D. C.; Einsle, O. Evidence for Interstitial Carbon in Nitrogenase FeMo Cofactor. *Science* **2011**, *334*, 940.

(8) Sluiter, M.: First Principles in Modelling Phase Transformations in Steels. In *Phase Transformations in Steels*; Pereloma, E., Edmonds, D., Eds.; Woodhead Publishing, 2017; pp 365−404.

(9) Bhadeshia, H. K. D. H. Cementite. *Int. Mater. Rev.* **2020**, *65*, 1−27.

(10) Grunenberg, J. The Interstitial Carbon of the Nitrogenase FeMo Cofactor Is Far Better Stabilized Than Previously Assumed. *Angew. Chem., Int. Ed.* **2017**, *56*, 7288−7291.

(11) McSkimming, A.; Harman, W. H. A Terminal N_2 Complex of High-Spin Iron(I) in a Weak, Trigonal Ligand Field. *J. Am. Chem. Soc.* **2015**, *137*, 8940−8943.

(12) Hoffman, B. M.; Lukoyanov, D.; Yang, Z. Y.; Dean, D. R.; Seefeldt, L. C. Mechanism of Nitrogen Fixation by Nitrogenase: The Next Stage. *Chem. Rev.* **2014**, *114*, 4041−4062.

(13) Doan, P. E.; Telser, J.; Barney, B. M.; Igarashi, R. Y.; Dean, D. R.; Seefeldt, L. C.; Hoffman, B. M. ^{57}Fe ENDOR Spectroscopy and 'Electron Inventory' Analysis of the Nitrogenase E4 Intermediate Suggest the Metal-Ion Core of FeMo-Cofactor Cycles through Only One Redox Couple. *J. Am. Chem. Soc.* **2011**, *133*, 17329−17340.

(14) Lukoyanov, D. A.; Yang, Z. Y.; Dean, D. R.; Seefeldt, L. C.; Raugei, S.; Hoffman, B. M. Electron Redistribution within the Nitrogenase Active Site FeMo-Cofactor During Reductive Elimination of H_2 to Achieve N≡N Triple-Bond Activation. *J. Am. Chem. Soc.* **2020**, *142*, 21679−21690.

(15) Pérez-González, A.; Yang, Z. Y.; Lukoyanov, D. A.; Dean, D. R.; Seefeldt, L. C.; Hoffman, B. M. Exploring the Role of the Central Carbide of the Nitrogenase Active-Site FeMo-Cofactor through Targeted ^{13}C Labeling and ENDOR Spectroscopy. *J. Am. Chem. Soc.* **2021**, *143*, 9183−9190.

(16) Weil, J. A.; Bolton, J. R.; Wertz, J. E.*Electron Paramagnetic Resonance: Elementary Theory and Practical Applications*; John Wiley & Sons, Inc: New York, 1994.

(17) Atherton, N. M.*Principles of Electron Spin Resonance*; Ellis Horwood: New York, 1993.

(18) Lukoyanov, D.; Pelmenschikov, V.; Maeser, N.; Laryukhin, M.; Yang, T. C.; Noodleman, L.; Dean, D.; Case, D.; Seefeldt, L.; Hoffman, B. Testing If the Interstitial Atom, X, of the Nitrogenase Molybdenum-Iron Cofactor Is N or C: ENDOR, ESEEM, and DFT Studies of the S = 3/2 Resting State in Multiple Environments. *Inorg. Chem.* **2007**, *46*, 11437−11449.

(19) Davis, L. C.; Henzl, M. T.; Burris, R. H.; Orme-Johnson, W. H. Iron-Sulfur Clusters in the Molybdenum-Iron Protein Component of Nigrogenase. Electron Paramagnetic Resonance of the Carbon Monoxide Inhibited State. *Biochemistry* **1979**, *18*, 4860−4869.

(20) Buscagan, T. M.; Perez, K. A.; Maggiolo, A. O.; Rees, D. C.; Spatzal, T. Structural Characterization of Two CO Molecules Bound to the Nitrogenase Active Site. *Angew. Chem., Int. Ed. Engl.* **2021**, *60*, 5704−5707.

(21) Barney, B. M.; Igarashi, R. Y.; Santos, P. C. D.; Dean, D. R.; Seefeldt, L. C. Substrate Interaction at an Iron-Sulfur Face of the FeMo-Cofactor During Nitrogenase Catalysis. *J. Biol. Chem.* **2004**, *279*, 53621−53624.

(22) Igarashi, R. Y.; Laryukhin, M.; Dos Santos, P. C.; Lee, H. I.; Dean, D. R.; Seefeldt, L. C.; Hoffman, B. M. Trapping H^- Bound to the Nitrogenase FeMo-Cofactor Active Site During H_2 Evolution: Characterization by ENDOR Spectroscopy. *J. Am. Chem. Soc.* **2005**, *127*, 6231−6241.

(23) Lukoyanov, D.; Barney, B. M.; Dean, D. R.; Seefeldt, L. C.; Hoffman, B. M. Connecting Nitrogenase Intermediates with the Kinetic Scheme for N_2 Reduction by a Relaxation Protocol and Identification of the N_2 Binding State. *Proc. Natl. Acad. Sci. U.S.A.* **2007**, *104*, 1451−1455.

(24) Hoeke, V.; Tociu, L.; Case, D. A.; Seefeldt, L. C.; Raugei, S.; Hoffman, B. M. High-Resolution ENDOR Spectroscopy Combined with Quantum Chemical Calculations Reveals the Structure of Nitrogenase Janus Intermediate E_4(4H). *J. Am. Chem. Soc.* **2019**, *141*, 11984−11996.

(25) Lukoyanov, D.; Khadka, N.; Yang, Z. Y.; Dean, D. R.; Seefeldt, L. C.; Hoffman, B. M. Reversible Photoinduced Reductive Elimination of H_2 from the Nitrogenase Dihydride State, the E_4(4H) Janus Intermediate. *J. Am. Chem. Soc.* **2016**, *138*, 1320−1327.

(26) Lee, H.-I.; Igarashi, R. Y.; Laryukhin, M.; Doan, P. E.; Dos Santos, P. C.; Dean, D. R.; Seefeldt, L. C.; Hoffman, B. M. An Organometallic Intermediate During Alkyne Reduction by Nitrogenase. *J. Am. Chem. Soc.* **2004**, *126*, 9563−9569.

(27) Igarashi, R. Y.; Dos Santos, P. C.; Niehaus, W. G.; Dance, I. G.; Dean, D. R.; Seefeldt, L. C. Localization of a Catalytic Intermediate Bound to the FeMo-Cofactor of Nitrogenase. *J. Biol. Chem.* **2004**, *279*, 34770−34775.

(28) Benton, P. M. C.; Laryukhin, M.; Mayer, S. M.; Hoffman, B. M.; Dean, D. R.; Seefeldt, L. C. Localization of a Substrate Binding Site on FeMo-Cofactor in Nitrogenase: Trapping Propargyl Alcohol with an α-70-Substituted MoFe Protein. *Biochemistry* **2003**, *42*, 9102−9109.

(29) Reed, A. E.; Curtiss, L. A.; Weinhold, F. Intermolecular Interactions from a Natural Bond Orbital, Donor-Acceptor Viewpoint. *Chem. Rev.* **1988**, *88*, 899−926.

(30) Cao, L.; Ryde, U. What Is the Structure of the E_4 Intermediate in Nitrogenase? *J. Chem. Theory Comput.* **2020**, *16*, 1936−1952.

(31) Thorhallsson, A. T.; Bjornsson, R. The E_2 State of FeMoco: Hydride Formation Versus Fe Reduction and a Mechanism for H_2 Evolution. *Chemistry* **2021**, *27*, 16788−16800.

(32) Hoffman, B. M.; Lukoyanov, D.; Dean, D. R.; Seefeldt, L. C. Nitrogenase: A Draft Mechanism. *Acc. Chem. Res.* **2013**, *46*, 587.

(33) Lukoyanov, D.; Khadka, N.; Dean, D. R.; Raugei, S.; Seefeldt, L. C.; Hoffman, B. M. Photoinduced Reductive Elimination of H_2 from the Nitrogenase Dihydride (Janus) State Involves a FeMo-Cofactor-H_2 Intermediate. *Inorg. Chem.* **2017**, *56*, 2233−2240.

(34) As cited in footnote 20 of ref 15.

(35) Jiménez-Vicente, E.; Del Campo, J. S. M.; Yang, Z. Y.; Cash, V. L.; Dean, D. R.; Seefeldt, L. C. Application of Affinity Purification Methods for Analysis of the Nitrogenase System from Azotobacter Vinelandii. *Methods Enzymol.* **2018**, *613*, 231−255.

(36) Christiansen, J.; Goodwin, P. J.; Lanzilotta, W. N.; Seefeldt, L. C.; Dean, D. R. Catalytic and Biophysical Properties of a Nitrogenase Apo-MoFe Protein Produced by a Nifb-Deletion Mutant of Azotobacter Vinelandii. *Biochemistry* **1998**, *37*, 12611−12623.

(37) Hoffman, B. M. ENDOR of Metalloenzymes. *Acc. Chem. Res.* **2003**, *36*, 522−529.

(38) DeRose, V. J.; Hoffman, B. M.: Protein Structure and Mechanism Studied by Electron Nuclear Double Resonance Spectroscopy. *Methods Enzymol*; Sauer, K., Ed.; Academic Press: New York, 1995; Vol. *246*; pp 554−589.

(39) Schweiger, A.; Jeschke, G. *Principles of Pulse Electron Paramagnetic Resonance*; Oxford University Press: Oxford, U.K., 2001.

(40) Doan, P. E.; Lees, N. S.; Shanmugam, M.; Hoffman, B. M. Simulating Suppression Effects in Pulsed ENDOR, and the 'Hole in the Middle' of Mims and Davies ENDOR Spectra. *Appl. Magn. Reson.* **2010**, *37*, 763−779.

(41) Raugei, S.; Seefeldt, L. C.; Hoffman, B. M. Critical Computational Analysis Illuminates the Reductive-Elimination Mechanism That Activates Nitrogenase for N_2 Reduction. *Proc. Natl. Acad. Sci. U.S.A.* **2018**, *115*, No. E10521.

(42) Smith, D.; Danyal, K.; Raugei, S.; Seefeldt, L. C. Substrate Channel in Nitrogenase Revealed by a Molecular Dynamics Approach. *Biochemistry* **2014**, *53*, 2278−2285.

(43) Becke, A. D. Density-Functional Exchange-Energy Approximation with Correct Asymptotic Behavior. *Phys. Rev. A: At., Mol., Opt. Phys.* **1988**, *38*, 3098−3100.

(44) Perdew, J. P. Density-Functional Approximation for the Correlation Energy of the Inhomogeneous Electron Gas. *Phys. Rev. B* **1986**, *33*, 8822−8824.

(45) Perdew, J. P. E. Density-Functional Approximation for the Correlation Energy of the Inhomogeneous Electron Gas. *Phys. Rev. B* **1986**, *34*, 7406.

(46) Becke, A. D. Density-Functional ThermochemistryIII The Role of Exact Exchange. *J. Chem. Phys.* **1993**, *98*, 5648−5652.

(47) Lee, C.; Yang, W.; Parr, R. G. Development of the Colle-Salvetti Correlation-Energy Formula into a Functional of the Electron Density. *Phys. Rev. B: Condens. Matter Mater. Phys.* **1988**, *37*, 785− 789.

(48) Stephens, P. J.; Devlin, F. J.; Chabalowski, C. F.; Frisch, M. J. Ab Initio Calculation of Vibrational Absorption and Circular Dichroism Spectra Using Density Functional Force Fields. *J. Phys. Chem.* **1995**, *98*, 11623−11627.

(49) Weigend, F.; Ahlrichs, R. Balanced Basis Sets of Split Valence, Triple Zeta Valence and Quadruple Zeta Valence Quality for H to Rn: Design and Assessment of Accuracy. *Phys. Chem. Chem. Phys.* **2005**, *7*, 3297−3305.

(50) Dolg, M.; Stoll, H.; Preuss, H. Energy-Adjusted Ab Initio Pseudopotentials for the Rare Earth Elements. *J. Chem. Phys.* **1989**, *90*, 1730−1734.

(51) Thorhallsson, A. T.; Benediktsson, B.; Bjornsson, R. A Model for Dinitrogen Binding in the E_4 State of Nitrogenase. *Chem. Sci.* **2019**, *10*, 11110−11124.

(52) Cao, L.; Ryde, U. Extremely Large Differences in DFT Energies for Nitrogenase Models. *Phys. Chem. Chem. Phys.* **2019**, *21*, 2480−2488.

(53) Jiang, H.; Ryde, U. Thermodynamically Favourable States in the Reaction of Nitrogenase without Dissociation of Any Sulfide Ligand. *Chem.—Eur. J.* **2022**, *28*, No. e202103933.

(54) Neese, F. The Orca Program System. *Wiley Interdiscip. Rev. Comput. Mol. Sci.* **2012**, *2*, 73−78.

(55) For further information about Orca, see: FACCTS. https://www.faccts.de/ (accessed on Aug 24, 2022).

(56) True, A. E.; Nelson, M. J.; Venters, R. A.; Orme-Johnson, W. H.; Hoffman, B. M. ^{57}Fe Hyperfine Coupling Tensors of the FeMo Cluster in Azotobacter Vinelandii MoFe Protein: Determination by Polycrystalline ENDOR Spectroscopy. *J. Am. Chem. Soc.* **1988**, *110*, 1935−1943.

(57) Hoffman, B. M.; Gurbiel, R. J.; Werst, M. M.; Sivaraja, M.: Electron Nuclear Double Resonance (ENDOR) of Metalloenzymes. In *Advanced EPR. Applications in Biology and Biochemistry*; Hoff, A. J., Ed.; Elsevier: Amsterdam, 1989; pp 541−591.

(58) Spatzal, T.; Einsle, O.; Andrade, S. L. A. Analysis of the Magnetic Properties of Nitrogenase FeMo Cofactor by Single-Crystal EPR Spectroscopy. *Angew. Chem., Int. Ed.* **2013**, *52*, 10116−10119.

(59) Abragam, A.; Bleaney, B. *Electron Paramagnetic Resonance of Transition Ions*; Dover Publications, Inc.: New York, 1986.

(60) Lukoyanov, D.; Yang, Z.-Y.; Dean, D. R.; Seefeldt, L. C.; Hoffman, B. M. Is Mo Involved in Hydride Binding by the Four-Electron Reduced (E_4) Intermediate of the Nitrogenase MoFe Protein? *J. Am. Chem. Soc.* **2010**, *132*, 2526−2527.

(61) Cameron, L. M.; Hales, B. J. Investigation of CO Binding and Release from Mo-Nitrogenase During Catalytic Turnover. *Biochemistry* **1998**, *37*, 9449−9456.

(62) Doan, P. E. Combining Steady-State and Dynamic Methods for Determining Absolute Signs of Hyperfine Interactions: Pulsed ENDOR Saturation and Recovery (PESTRE). *J. Magn. Reson.* **2011**, *208*, 76−86.

(63) Sippel, D.; Rohde, M.; Netzer, J.; Trncik, C.; Gies, J.; Grunau, K.; Djurdjevic, I.; Decamps, L.; Andrade, S. L. A.; Einsle, O. A Bound Reaction Intermediate Sheds Light on the Mechanism of Nitrogenase. *Science* **2018**, *359*, 1484−1489.

(64) Rohde, M.; Sippel, D.; Trncik, C.; Andrade, S. L. A.; Einsle, O. The Critical E_4 State of Nitrogenase Catalysis. *Biochemistry* **2018**, *57*, 5497−5504.

(65) Pelmenschikov, V.; Case, D. A.; Noodleman, L. Ligand-Bound S = 1/2 FeMo-Cofactor of Nitrogenase: Hyperfine Interaction Analysis and Implication for the Central Ligand X Identity. *Inorg. Chem.* **2008**, *47*, 6162−6172.

(66) Mouesca, J. M.; Noodleman, L.; Case, D. A. Analysis of the ^{57}Fe Hyperfine Coupling Constants and Spin States in Nitrogenase P-Clusters. *Inorg. Chem.* **1994**, *33*, 4819−4830.

(67) Badding, E.; Srisantitham, S.; Lukoyanov, D.; Hoffman, B.; Suess, D. Connecting the Geometric and Electronic Structures of the Nitrogenase Iron−Molybdenum Cofactor through Site-Selective Labeling, **2022**, ChemRxiv; Cambridge Open Engage: Cambridge, 2022; pp 1-28 (accessed on Aug 25, 2022).

(68) Lukoyanov, D. A.; Krzyaniak, M. D.; Dean, D. R.; Wasielewski, M. R.; Seefeldt, L. C.; Hoffman, B. M. Time-Resolved EPR Study of H_2 Reductive Elimination from the Photoexcited Nitrogenase Janus E_4(4H) Intermediate. *J. Phys. Chem. B* **2019**, *123*, 8823−8828.

(69) Einsle, O.; Rees, D. C. Structural Enzymology of Nitrogenase Enzymes. *Chem. Rev.* **2020**, *120*, 4969−5004.

NOTE ADDED AFTER ASAP PUBLICATION

This paper was published ASAP on September 27, 2022, with errors in the Figure 7 caption. The corrected version was reposted on September 30, 2022.